Background Velocity Inversion by Phase along Reflection Wave Paths

Han Yu, Bowen Guo, and Gerard T. Schuster, King Abdullah University of Science and Technology (KAUST)*

Summary

A background velocity model containing the correct low-wavenumber information is desired for both the quality of the migration image and the success of waveform inversion. We propose to invert for the low-wavenumber part of the velocity model by minimizing the phase difference between predicted and observed reflections. The velocity update is exclusively along the reflection wavepaths and, unlike conventional FWI, not along the reflection ellipses. This allows for reconstructing the smoothly varying parts of the background velocity model. Tests with synthetic data show both the benefits and limitations of this method.

Introduction

Full waveform inversion (FWI) has attracted a great deal of research effort for both space-time and space-frequency methods (Tarantola, 1984, 1986; Pratt et al., 1998). It has also been successfully applied to some data sets (Sirgue and Pratt, 2004; Sheng et al., 2006; Shin and Min, 2006), but its success largely depends on the accuracy of the initial velocity model. A small deviation of this initial tomogram may degrade the travel time information and consequently the migration image quality. Thus, obtaining a good background velocity model is a fundamental requirement for seismic inversion (Virieux and Operto, 2009).

Traveltime tomography methods (Zhu and McMechan, 1989; Pratt and Goulty, 1991; Aki and Richards, 2002) can provide a relatively reliable background velocity model for FWI that inverts only the early arrivals. The depth of the velocity model that traveltime tomography can invert for depends on the maximal source-to-receiver offset. Recently, Xu et al. (2012) proposed to boost the low-wavenumber component for updating the velocity model by singling out the reflection wave paths, thereby allowing the inversion for deep parts of the model without long offset data. This method mainly focuses on inverting the background velocity (Qin et al., 2013; Wang et al., 2013), rather than generating a highly resolved tomogram. The velocity model is decoupled into a transmissive component plus a reflective component. These two components are updated in turn while fixing the other. At each iteration, the image is firstly migrated from the data and then demigrated based on the obtained image to obtain the difference between the observed and the demigrated data. This difference is then smeared back along the wave paths for the gradient.

Previous methods for calculating the data residual use either direct subtraction or cross correlation (Luo and Schuster, 1991) between the predicted and the observed data. In this work, we adopt a method proposed by Sun and Schuster (1993) to mitigate the amplitude difference and reinforce the phase difference in the two data sets. We will present the theory and work flow first, and then show the numerical results. The final section is the conclusion.

Theory and Work Flow

Without loss of generality, we treat the subsurface velocity distribution $v(\mathbf{x})$ as the combination of a background velocity model $v_0(\mathbf{x})$ and a reflectivity model $\delta v(\mathbf{x})$ such that

$$v(\mathbf{x}) = v_0(\mathbf{x}) + \delta v(\mathbf{x}). \quad (1)$$

To update $v_0(\mathbf{x})$ using the reflection wave paths is to minimize the following waveform misfit function (Xu et al., 2012)

$$E = \min \tfrac{1}{2} \| d_{obs} - d_{obs} \|^2, \quad (2)$$

where d_{obs} denotes the observed data mostly consisting of the reflection energy, and d_{calc} denotes the demigrated data using the Born approximation. The Fréchet derivative $\partial E/\partial v_0(\mathbf{x})$ is equal to the wave paths that can be migrated in the reverse time sense (Xu et al., 2012).

To construct the misfit gradient, we start from the acoustic wave equation in the space-time ($\mathbf{x}$-t) domain

$$1/ v_0^2(\mathbf{x})\, \partial^2 p(\mathbf{x}, t|\mathbf{x}_s)/\partial t^2 - \Delta p(\mathbf{x}, t|\mathbf{x}_s) = src(\mathbf{x}_s, t), \quad (3)$$

where $p(\mathbf{x}, t|\mathbf{x}_s)$ denotes the pressure field trace recorded at the subsurface position $\mathbf{x}$, with listening time t and a source at $\mathbf{x}_s$. For simplicity, we will use s and r to respectively represent the source position $\mathbf{x}_s$ and the receiver position $\mathbf{x}_r$ in this paper. The first step of inversion is to migrate d_{obs} with the initial velocity model $v_0^{(1)}(\mathbf{x})$ based on equation 3 to obtain the image $m(\mathbf{x})$. This migration image m is then used to generate the demigrated data d_{calc} with the Lippmann-Schwinger equation under the Born approximation. The data mismatch Δd between d_{obs} and d_{calc} is estimated to create the virtual sources for the back propagation. To calculate the reflection wave paths, the back propagated wavefields are correlated with the forward wavefields at zero-lag. So the overall gradient consists of two parts: one from the source to the image and the other from the image to the receiver (Figure 1).

DOI http://dx.doi.org/10.1190/segam2014-0011.1

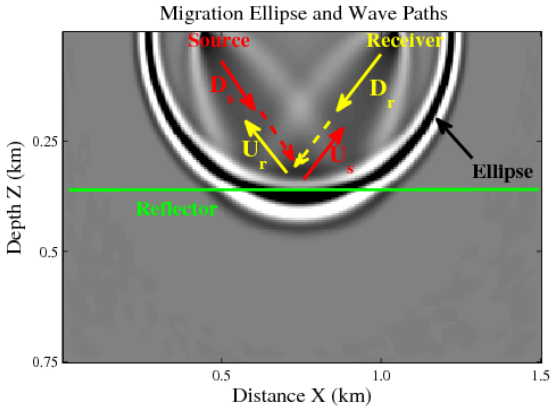

Figure 1: The migration ellipse and wave paths.

Based on this method, the background velocity model v_0 can be updated along the wave paths from the shot locations to reflectors, and then back to the receiver positions. This work flow can be summarized in the frequency domain as follows:

$$S_0\text{: } m(\mathbf{y}) = \Sigma_{s,r}\, \omega^2\, D_{obs}(r|s)\, (W(\omega)G(\mathbf{y}|s)G(\mathbf{y}|r))^*, \quad (4a)$$

$$S_1\text{: } U_s(\mathbf{x}) = \Sigma_{\mathbf{y},s}\, \omega^2\, G(\mathbf{x}|\mathbf{y})\, m(\mathbf{y})W(\omega)G(\mathbf{y}|s), \quad (4b)$$

$$S_2\text{: } D_r(\mathbf{x}) = \Sigma_{s,r}\, \Delta D^*(r|s)\, G(\mathbf{x}|r), \quad (4c)$$

$$S_3\text{: } U_r(\mathbf{x}) = \Sigma_{\mathbf{y},s,r}\, G(\mathbf{x}|\,\mathbf{y})\, m(\mathbf{y})\, \Delta D^*(r|s)\, G(\mathbf{y}|r), \quad (4d)$$

$$S_4\text{: } D_s(\mathbf{x}) = \Sigma_s\, \omega^2\, W(\omega)\, G(\mathbf{x}|s), \quad (4e)$$

$$S_5\text{: } v_0^{(n+1)}(\mathbf{x}) = v_0^{(n)}(\mathbf{x}) - \alpha\Sigma_\omega\, (D_r U_s^* + D_s U_r^*). \quad (4f)$$

In equations 4a to 4f, the up and down going waves are respectively represented by U and D; ω denotes the angular frequency and $W(\omega)$ is the source spectrum; $G(\mathbf{y}|s)$ is the Green's function from the source to $\mathbf{y}$ associated with equation 3 provided the source term is the Delta function. The reflection wave paths can be clearly discerned in Figure 1 and the migration ellipse is dropped for the inversion.

However, to calculate the step length α, it is still necessary to compare D_{obs} with D_{calc} in order to determine if the newly updated $v_0(\mathbf{x})$ is better than from the previous iteration. Therefore, the migration and demigration procedures need to be revisited again, which is very time consuming. Errors between the finite difference data and the demigrated data (Woodward, 1989) indicate that a direct subtraction may not be a good strategy. Here, to strengthen the phase and weaken the amplitude in the data residual, we only estimate their phase difference using the method proposed by Sun and Schuster (1993). For any pair of source s and receiver r, both the recorded trace d_{obs} and the calculated trace d_{calc} are Fourier transformed (F) to obtain their amplitude spectrum and phase spectrum θ,

$$D_{obs}(r|s) = F(d_{obs}(r|s)) = A_{obs}(r,\omega;s)\, \exp[i\theta_{obs}(r,\omega;s)], \quad (5a)$$

$$D_{calc}(r|s) = F(d_{calc}(r|s)) = A_{calc}(r,\omega;s)\, \exp[i\theta_{calc}(r,\omega;s)]. \quad (5b)$$

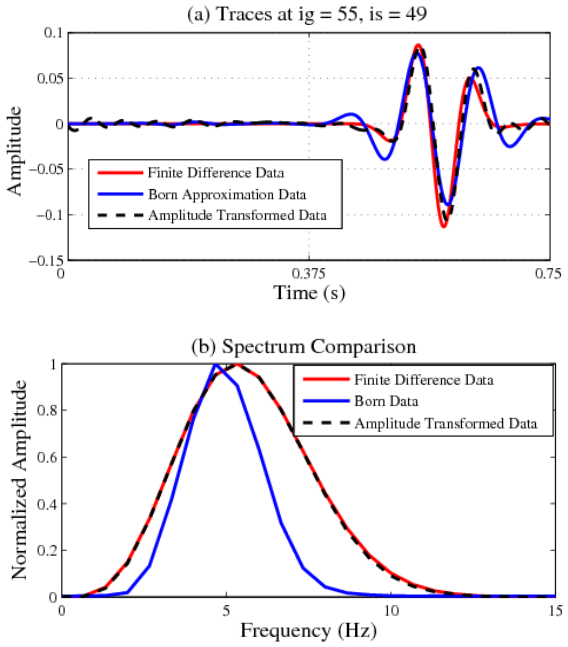

Figure 2: (a) The reflection data calculated by finite difference scheme, the demigration data calculated by Born modeling, and the transformed demigration data using equation 7; (b) their spectrum. The data for comparison are calculated based on a two layered velocity model.

The amplitude spectra of the calculated trace A_{calc} is replaced by the amplitude of the observed trace A_{obs}, so there is only a phase mismatch in the residual. This can be quickly implemented in the frequency domain. Therefore, we define a new data misfit functional

$$\bar{E} = min\ ½\ \|\Delta\bar{d}\|^2 = min\ ½\ \|\, d_{obs} - \bar{d}_{calc}\|^2, \quad (6)$$

where

$$\bar{d}_{calc} = F^{-1}(A_{obs}\, exp(i\theta_{calc})), \quad (7)$$

and thereby avoid the direct subtraction $\Delta d = d_{obs} - d_{calc}$. Using this transformation, the observed data and the demigrated data can be matched more easily. This is illustrated in Figure 2 based on a two layered velocity

DOI http://dx.doi.org/10.1190/segam2014-0011.1

model. In theory, the conventional misfit gradient $\partial E/\partial v_0(\mathbf{x})$ is not valid for the phase inversion, but we still plug the new data residual $\Delta\bar{d}$ into $\partial E/\partial v_0(\mathbf{x})$ for back propagation as an approximation to the real gradient $\partial \bar{E}/\partial v_0(\mathbf{x})$.

Numerical Experiment

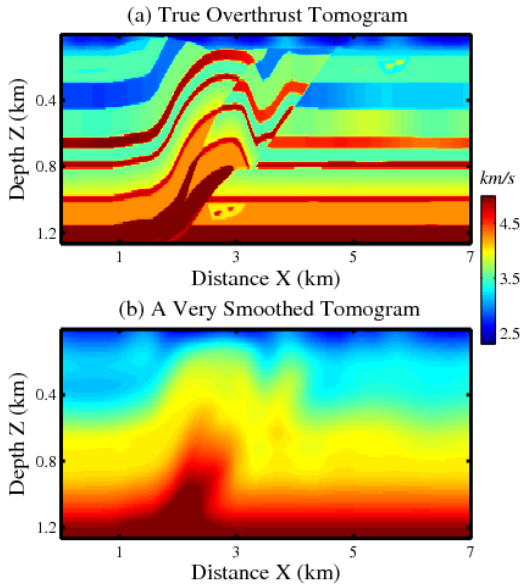

Figure 3: The (a) true and the (b) smoothed Overthrust velocity models.

A synthetic test is carried out for a vertical 2D portion of the overthrust model, where Figure 3(a) is used to generate the observed data d_{obs} in the time-space domain. The velocity model is a 126×701 gridded mesh with a 10 *m* grid spacing. We resort to low-frequency data which is generated by a 2nd order in time and 8th order in space finite-difference scheme (Levander, 1988) with a Ricker wavelet peaked at 5 Hz. The recording time is 1.5 *s* with a temporal sampling of 1 *ms*. There are altogether 88 shots with a shot spacing 80 *m*, where each shot corresponds to the same fixed 175 receivers with a receiver spacing 40 *m*. The initial model is a 1D-velocity model (Figure 4(a)) extracted from a vertical slice of a smoothed version (Figure 3(b)) of the original velocity model.

The inverted tomograms are shown in Figures 4(b-d). Figure 4(d) shows the tomogram using direct subtraction $d_{obs} - d_{calc}$ as the back propagated virtual sources, whereas Figure 4(c) presents the tomogram using $d_{obs} - \bar{d}_{calc}$ for phase inversion. The protruding structure at $x = 2$ *km* and $z = 0.8$ *km* can be distinguished in Figures 4(b) and 4(c) while it is obscure in Figure 4(d). The normalized data residuals associated with Figures 4(c) and 4(d) both decrease to 50%, which implies that the data misfit can be less sensitive to the velocity perturbation. Figure 4(c) can also serve as the initial velocity model for conventional FWI. A direct comparison between Figures 4(b) and 4(c) is somewhat inappropriate since one inverts for details plus background information while the other concentrates on the background velocity inversion.

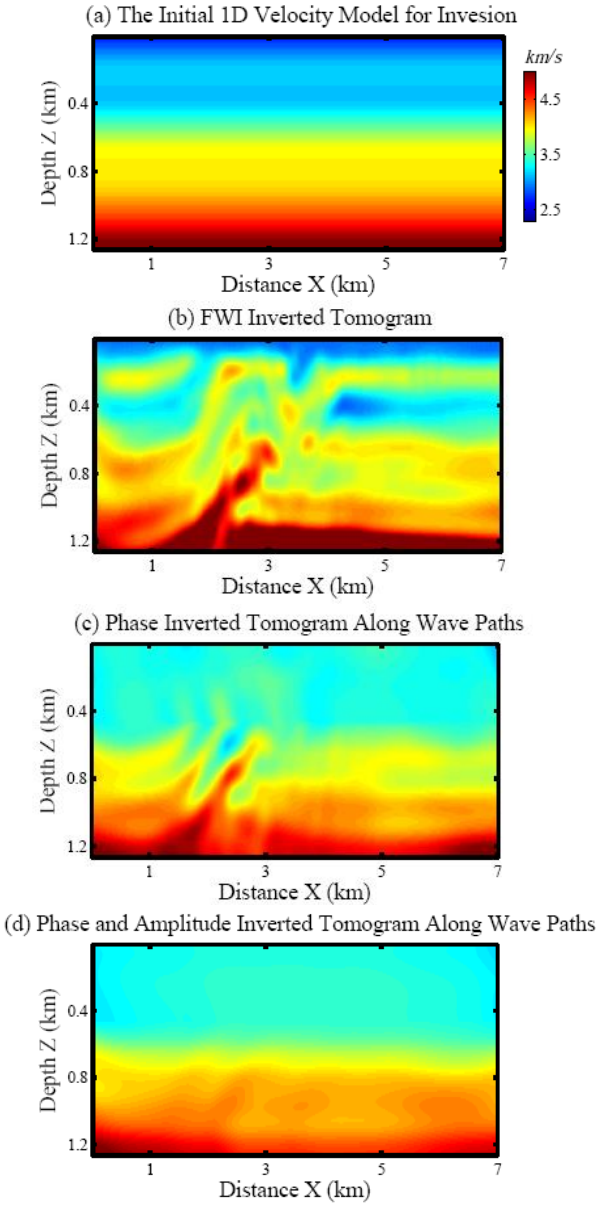

Figures 4: (a) The 1D initial velocity model, the tomograms inverted by (b) conventional FWI, by (c) only phase along

DOI http://dx.doi.org/10.1190/segam2014-0011.1

reflection wave paths, and by (d) both amplitude and phase along reflection wave paths.

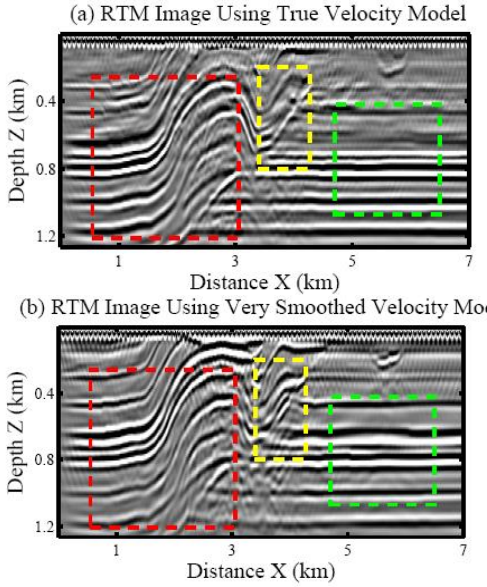

Figure 5: RTM images using (a) the true overthurst velocity model, and (b) its very smoothed version.

The migration images with the true and smoothed velocity models are presented in Figure 5, where Figures 5(a) and 5(b) are very close to each other, demonstrating the importance of a good background velocity model for migration. The migration images (Figure 6) with the inverted tomograms use a data set generated by a Ricker wavelet peaked at 25 Hz. Referring to Figure 5(a), it is obvious that many subsurface details can be imaged in Figure 6(c) compared with Figures 6(a) and 6(d), suggesting the effectiveness of phase inversion. Figure 6(b) with conventional FWI tomogram shows a better migration image than other three. Nevertheless, the image closest to Figure 6(b) is still 6(c).

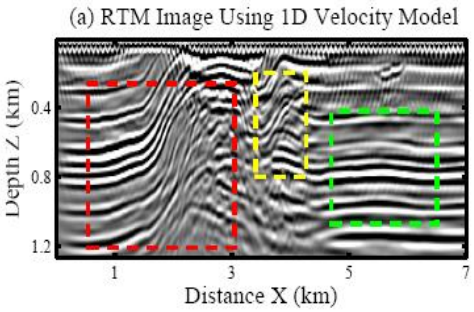

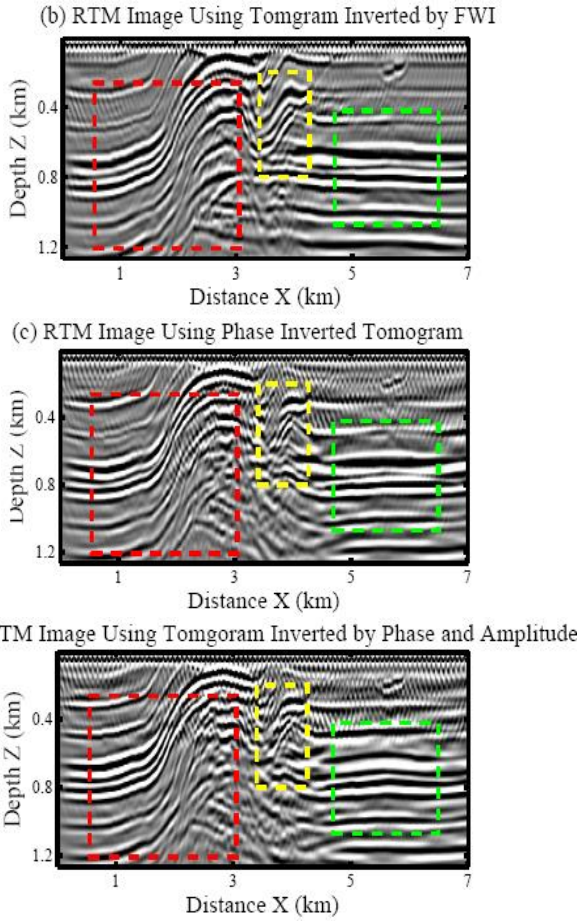

Figure 6: RTM images using (a) the 1D initial velocity model, the tomograms inverted by (b) conventional FWI, by (c) only phase along reflection wave paths, and by (d) both amplitude and phase along reflection wave paths.

Conclusions

We implement the reflection based waveform inversion by updating the background velocity model along the low-wavenumber reflection wave paths and taking advantage of matching the phase between the observed and the demigrated data. Therefore it promises to reconstruct the low wavenumber parts of the velocity model to mitigate cycle skipping problems. Results with synthetic data show that it improves the quality of the migration image, but the data misfit is less sensitive to the perturbation of the background velocity model. I hope to apply this method to phase inversion in the image domain.

Acknowledgements
The computation resource Shaheen for inversion provided by KAUST is greatly appreciated.

DOI http://dx.doi.org/10.1190/segam2014-0011.1

http://dx.doi.org/10.1190/segam2014-0011.1

EDITED REFERENCES

Note: This reference list is a copy-edited version of the reference list submitted by the author. Reference lists for the 2014 SEG Technical Program Expanded Abstracts have been copy edited so that references provided with the online metadata for each paper will achieve a high degree of linking to cited sources that appear on the Web.

REFERENCES

Aki, K., and P. G. Richards, 2002, Quantitative seismology, 2nd ed.: University Science Books.

Levander, A. R., 1988, Fourth-order finite-difference P-SV seismograms: Geophysics, **53**, 1425–1436, http://dx.doi.org/10.1190/1.1442422.

Luo, Y., and G. T. Schuster, 1991, Wave equation traveltime inversion: Geophysics, **56**, 645–653, http://dx.doi.org/10.1190/1.1443081.

Pratt, R. G., and N. R. Goulty, 1991, Combining wave-equation imaging with traveltime tomography to form high-resolution images from crosshole data: Geophysics, **56**, 208–224, http://dx.doi.org/10.1190/1.1443033.

Pratt, R. G., C. Shin, and Hicks, 1998, Gauss-Newton and full Newton methods in frequency space seismic waveform inversion: Geophysical Journal International, **133**, no. 2, 341–362, http://dx.doi.org/10.1046/j.1365-246X.1998.00498.x.

Qin, F., T. W. Fei, and Y. Luo, 2013, Velocity model building from waveform tomography of band limited reflection seismic data: 83rd Annual International Meeting, SEG, Expanded Abstracts, 866–871.

Sheng, J., A. Leeds, M. Buddensiek, and G. T. Schuster, 2006, Early arrival waveform tomography on near-surface refraction data: Geophysics, **71**, no. 4, U47–U57, http://dx.doi.org/10.1190/1.2210969.

Shin, C., and D. J. Min, 2006, Waveform inversion using a logarithmic wavefield: Geophysics, **71**, no. 3, R31–R42, http://dx.doi.org/10.1190/1.2194523.

Sirgue, L., and R. G. Pratt, 2004, Efficient waveform inversion and imaging: A strategy for selecting temporal frequencies: Geophysics, **69**, 231–248, http://dx.doi.org/10.1190/1.1649391.

Sun, Y., and G. T. Schuster, 1993, Time-domain phase inversion: 63rd Annual International Meeting, SEG, Expanded Abstracts, 684–687.

Tarantola, A., 1984, Inversion of seismic reflection data in the acoustic approximation: Geophysics, **49**, 1259–1266, http://dx.doi.org/10.1190/1.1441754.

Tarantola, A., 1986, A strategy for nonlinear elastic inversion of seismic reflection data: Geophysics, **51**, 1893–1903.

Virieux, J., and S. Operto, 2009, An overview of full-waveform inversion in exploration geophysics: Geophysics, **74**, no. 6, WCC1–WCC26, http://dx.doi.org/10.1190/1.3238367.

Wang, S., F. Chen, H. Zhang, and Y. Shen, 2013, Reflection-based full waveform inversion (RFWI) in the frequency domain: 83rd Annual International Meeting, SEG, Expanded Abstracts, 877–881.

Woodward, M. J., 1989, Wave-equation tomography: Ph.D. dissertation, Stanford University.

Xu, S., D. Wang, F. Chen, Y. Zhang, and G. Lambare, 2012, Full waveform inversion for reflected seismic data: 74th Conference & Exhibition, EAGE, Extended Abstracts, W024.

Zhu, X., and G. A. McMechan, 1989, Estimation of a two-dimensional seismic compressional-wave velocity distribution by iterative tomographic imaging: International Journal of Imaging Systems and Technology, **1**, no. 1, 13–17, http://dx.doi.org/10.1002/ima.1850010103.